Failure of a brittle layer on a ductile substrate: Nanoindentation experiments and FEM simulations

M. Rusinowicz, G. Parry, F. Volpi, D. Mercier, S. Eve, Ulrike Lüders, F. Lallemand, M. Choquet, M. Braccini, C. Boujrouf, et al.

To cite this version:

M. Rusinowicz, G. Parry, F. Volpi, D. Mercier, S. Eve, et al.. Failure of a brittle layer on a ductile substrate: Nanoindentation experiments and FEM simulations. Journal of the Mechanics and Physics of Solids, 2022, 163, pp.104859. 10.1016/j.jmps.2022.104859 . hal-03708224

HAL Id: hal-03708224
https://hal.science/hal-03708224v1

Submitted on 4 Oct 2022

Failure of a brittle layer on a ductile substrate: Nanoindentation experiments and FEM simulations

M. Rusinowicz[1], G. Parry[1], F. Volpi[1], D. Mercier[2], S. Eve[3], U. Lüders[3], F. Lallemand[4], M. Choquet[4], M. Braccini[1], C. Boujrouf[1], E. Hug[3], R. Coq Germanicus[3], M. Verdier[1]

[1] *Univ. Grenoble Alpes, CNRS, Grenoble INP, SIMaP, F-38000 Grenoble, France*
[2] *Ansys Inc., Materials BU, 69100 Villeurbanne, France*
[3] *Normandie Univ., ENSICAEN, UNICAEN, CNRS, CRISMAT, 14000 Caen, France*
[4] *Murata Integrated Passive Solutions, 2 Rue De La Girafe, 14000 Caen, France*

Abstract

Functional devices such as microelectronic systems, solar cells and power devices are composed of complex stacks of various materials, including semiconductors, ceramics and metallic alloys. The knowledge of the mechanical response of those stacks is a key point, as they are submitted to harsh stresses during the fabrication process (induced by thermal treatments, mechanical polishing, packaging processes, ...) as well as during the device lifetime.

We report the mechanical study of a microelectronic-dedicated stack where a silicon nitride (Si_3N_4) layer was deposited on top of a thick metallic alloy ($AlSiCu$) layer. In microelectronic chips, Si_3N_4 is widely used as a passivation layer, while $AlSiCu$ is the electrical connection layer. The structure has been tested experimentally by nanoindentation. Multiple pop-in events were observed on the loading curves, indicating multiple cracking, with cracks initiated at various loading stages. The high reproducibility of the loading curves then allowed their full analysis by numerical modelling.

The complete damage process of the multilayer during indentation is analyzed using modelling by the Finite Element Method (FEM), accounting for plasticity in $AlSiCu$, crack propagation in the Si_3N_4 layer and possible delamination at the interface between the two layers. The various stages of the damage process occurring in the Si_3N_4 are elucidated, showing in particular the occurrence of a first crack in the region underneath the indenter (hence not visible by a surface observation), followed by a second crack forming further away from the indenter, on the top surface of the layer. Moreover, a novel procedure for the identification of the Si_3N_4 layer tensile strength is presented, using an inverse method based on FEM simulations and experimental data. The results of the simulations (cracking patterns and cracks locations) are also further validated by the observation of structure cross-sections with a Scanning Electron Microscope (SEM) after Focused Ion Beam (FIB) milling of the sample. In addition, the proposed identification procedure is quite generic and can be adapted to other systems showing similar multiple-cracking patterns under indentation.

Keywords: Nanoindentation, Fracture, Multilayers, FEM simulations, X-FEM,

1. Introduction

In the field of functional applications, devices are manufactured using planar technologies that proceed with successive cycles of film deposition, patterning and etching processes. This process flow results in complex stacks of thin films that combine different families of materials (semiconductors, dielectrics, metals) with dissimilar properties. A typical example of such multilayer stacks can be found at the top surface of most microelectronic chips, where a silicon nitride (Si_3N_4) film is generally deposited on top of the whole device stack at the final processing step. This layer is an efficient passivation layer against moisture and ambient contaminants (Aberle, 2000; Lin, 2011; Morin et al., 2011; Kaloyeros et al., 2017; Cazako et al., 2018). In standard process flows, it is deposited by Plasma Enhanced Chemical Vapor Deposition (PECVD) (Kaloyeros et al., 2017; Gan et al., 2018; Xiang et al., 2019), and fully covers the wafer surface. Depending on the device layout, this dielectric Si_3N_4 film can be locally deposited on top of a metallic alloy ($'brittle-on-ductile'$ stack) or another dielectric film ($'brittle-on-brittle'$ stack). During processing, these wafers are subjected to the mechanical stresses induced by packaging processes (grinding, dicing, bumping, ball dropping, cleaving or sawing) (Bustillo et al., 1998; Tekin, 2011) and to the thermal stresses that build up during device operation (Sinha et al., 1978; Evans et al., 1998; Raghavan et al., 2016). These stresses may initiate and propagate some mechanical cracks that can lead to device failures. Preventing these stress-induced failures requires to properly apprehend the mechanical behavior of these multi-material stacks. In particular, a robust design of these systems requires the quantitative knowledge of the fracture properties of constitutive layers. In literature, the mechanical properties of Si_3N_4 layers with different under-layers have been explored for mechanically hard sub-layers (silicon, fused silica, germanium and sapphire) (Soh et al., 2006), showing a strong influence of the substrate on hardness measurements. To the best of our knowledge, the mechanical properties on mechanically soft under-layers were studied only very scarcely. Scafidi and Ignat (Scafidi and Ignat, 1998) have studied the crack propagation with *in situ* tensile tests of PECVD Si_3N_4 deposited on Al substrates, focusing on the different steps of the damage using a simplified analytical approach with a shear lag model. However, in the context of high-integrated microelectronic devices, in order to optimize the process flow, investigation is needed to determine the critical tensile stress of deposited Si_3N_4 as coating layer.

As already stated, the mechanical behavior of such thin film stacks is a cornerstone question that numerous application fields have to address, as for the development of microelectronic chips, solar cells, embedded power devices, optical lens functionalization, thermal barrier coatings, and surface hardening of cutting tools. However, measuring material properties of such structures remains a difficult task, because of their composite response. In terms of experimental means, nanoindentation is a mechanical testing technique well suited for the determination of the intrinsic mechanical parameters of single materials (Lin et al., 2009) or thin films deposited on a substrate (Li and Vlassak, 2009; Li et al., 2003; Liu et al., 2015). A review of the methods for extracting mechanical properties of coatings from nanoindentation load–displacement curves is proposed in (Bull, 2005). Nanoindentation shows to be particularly useful for investigating the properties of multiple stacks (Chen and Bull, 2006; Wang et al., 2016). The measurement of hardness and elastic moduli from nanoindentation can be obtained in both cases of $'hard-coating-on-softer-substrates'$ (Saha and Nix, 2002) and of $'soft-coating-on-harder-substrates'$ (Beegan et al., 2004), but numerical simulations are required to identify the material properties from experimental data (Pelegri and Huang, 2008; Sakai, 2009). The problem of determining the fracture properties (i.e. fracture strength, fracture toughness) of coatings is even more challenging. Although there is no standard test procedure to date, there are however several methods used by researchers to try to access to these quantities, either stress-based or energy-based methods (Zhang et al., 2005). Indenting the coating in order to propagate cracks is maybe the most widely used method. But there are quite a few difficulties inherent to this method, such as (non exhaustively) the formation of the precrack, the determination of the crack length, the critical failure stress, and the development of plastic deformations in the substrate during loading process. In this context, modelling by the Finite Element Method (FEM) can be used to simulate crack initiation and propagation during indentation, and to compare the loading curves obtained numerically to the ones obtained experimentally, in order to identify key parameters such as the fracture toughness of the coatings (Kot et al., 2013; Fukumasu and Souza, 2014; Lofaj and Németh, 2017).

In this study, the analysis of the fracture behavior of a $Si_3N_4/AlSiCu/SiO_2/Si$ multilayer system under nanoindentation is reported. The evidence of successive displacement bursts ('pop-in') can be observed on the loading curves. Numerical FEM calculations are carried out accounting for: 1) plastic deformation in the $AlSiCu$ layer, 2) crack initiation and propagation inside the Si_3N_4 layer, using Extended-FEM (X-FEM) combined with a cohesive behavior of the cracks, 3) a possible delamination at the $Si_3N_4/AlSiCu$ interface using a cohesive zone model. The behavior of the $AlSiCu$ underlayer in the plastic deformation regime is also identified by fitting parameters in FEM simulations using nanoindentation results and *post mortem* images of imprints. The various stages of the damage process occurring in the Si_3N_4 layer are elucidated thanks to numerical simulation, showing in particular the occurrence of a first crack in the region underneath the indenter (hence not visible by a surface observation), followed by a second crack forming on the top surface of the layer, further from the indenter. Moreover, a novel procedure for the identification of the Si_3N_4 layer tensile strength is presented, using an inverse method based on FEM simulations and experimental data. This approach uses the distance of the first crack to the indenter axis as well as the tensile strength as parameters involved in the optimization procedure. The consistency with experimental data is extremely good and allows to narrow down the possible values of the tensile strength. Finally, the results of simulations (cracking patterns and crack locations) are also further validated using a Scanning Electron Microscope (SEM) cross-section view of the sample. The identification procedure is quite generic and can be adapted to other systems showing similar multiple-cracking patterns under indentation.

2. Experimental details

2.1. Samples

The investigated structure is a multi-material film stack usually designed in microelectronic chips for high-integrated systems. The starting material is a (001)-oriented 6" single crystal silicon wafer with a thickness of 675 μm. After substrate cleaning, a 450 nm thick SiO_2 layer was deposited by PECVD followed by the sputtering of $Al_{98.96}Si_{1.00}Cu_{0.04}$ ($AlSiCu$) polycrystalline metallic alloy. Finally a Si_3N_4 amorphous film was deposited by PECVD at low temperature (about 400 $^\circ C$) using a SiH_4/NH_3 gas mixture. The deposition rate was about 0.2 $\mu m/min$ with a SiH_4/NH_3 flow ratio of 0.15. The RF power was optimized at 400 W with a chamber pressure of 2.7 $Torr$. The layer thickness and chemical compositions were verified by SEM and Energy Dispersive X-ray (EDX) analysis. A SEM cross-sectional view of the sample is shown in Fig. 1. The thickness of the deposited $AlSiCu$ and Si_3N_4 films were 3.0 ± 0.1 μm and 1.3 ± 0.1 μm, respectively.

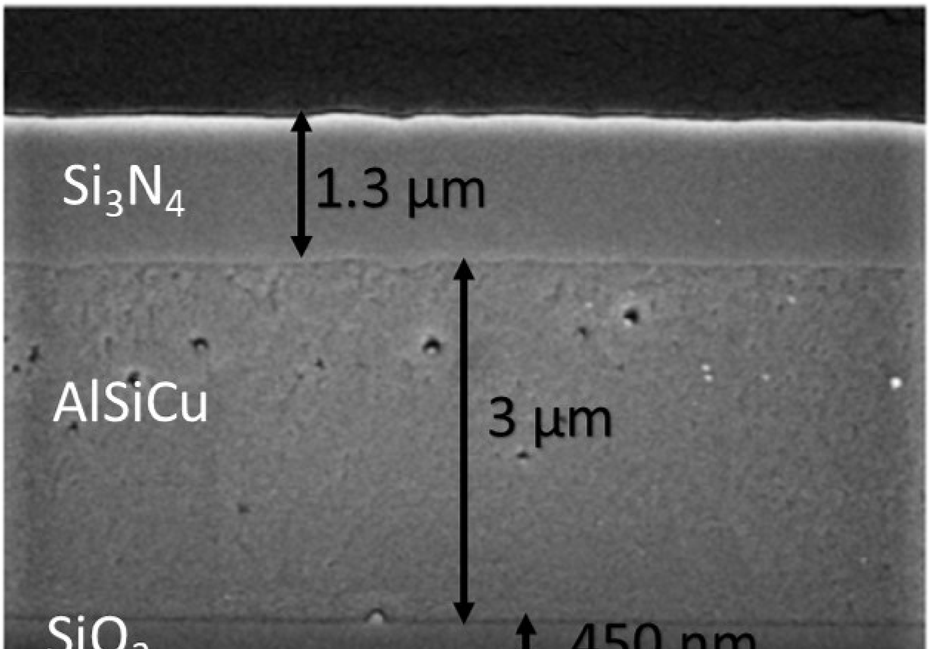

Figure 1: Cross-sectional SEM view of the investigated structure.

2.2. Experimental techniques: Nanoindentation and residual imprint observations

Two nanoindentation systems were used. The first apparatus was an InForce 50 actuator (from Nanomechanics Inc. / KLA-Tencor) integrated into a home-made set-up and the second one was an MTS Nano Indenter XP. Both apparatuses operate in a *load-controlled* mode. Tests were performed at a strain rate of 0.05 s^{-1}. Berkovich diamond tips were used, with nominal tip radius of ≈ 20 nm for both tips. In both apparatuses, the Continuous Stiffness Measurement (CSM) mode was used, thus allowing continuous hardness and elasticity extraction during indentation. Spacing between indents was fixed to several tens of μm, thus avoiding any overlapping of deformation fields. The displacement data were corrected from drift rate which was re-evaluated before or after each test.

Residual nanoindentation imprints were essentially observed by SEM, before or after Focused Ion Beam (FIB) milling. Two systems were used: a FIB Cross Beam NVision 40 from Carl Zeiss (Ga source with an acceleration voltage of 30 kV and current intensity of 300 pA) and a SEM Zeiss Supra 55 operated at 5 kV. Imprint observations were also performed by Atomic Force Microscopy (AFM) on an AFM ICON (Bruker, Corporation, USA) in the scan-asyst mode.

3. Experimental results

3.1. Nanoindentation tests

Fig. 2 shows representative loading curves obtained from the indentation of the $Si_3N_4/AlSiCu/SiO_2/Si$ stack (load versus penetration depth normalized by the Si_3N_4 film thickness). Fig. 2.a and 2.b report the data from tests performed at maximum loads of 15 mN and 45 mN, respectively. On these curves, significant displacement jumps at constant load, called 'pop-in' events can be observed. As nanoindentation tests are performed in a *load-controlled* mode, these horizontal plateaus correspond to abrupt displacement bursts of the indenter into the sample when the sample compliance suddenly changes. In Fig. 2.b, two pop-ins can be distinguished: the first pop-in starts for a critical (depth ; load) dataset of ($h_{c1} = 266 \pm 21$ nm ; $L_{c1} = 11.8 \pm 1.1$ mN) and ends at a final depth of $h_{f1} = 356 \pm 46$ nm. For the second pop-in, values are much more dispersed: $h_{c2} = 694 \pm 116$ nm, $L_{c2} = 23.1 \pm 3.6$ mN, $h_{f2} = 790 \pm 86$ nm. It is worth noting that, when loading ends at 15 mN, only the first pop-in can be observed (Fig. 2.a).

3.2. SEM observations

Generally, pop-in events can be the signature of different phenomena such as the nucleation of dislocations (Gaillard et al., 2003), stressed-induced phase transformation (Bradby et al., 2002), twinning (Jian et al., 2013), film cracking (Li et al., 1997; Bull, 2005). In $'brittle-film-on-elastic-plastic-substrate'$ stacks, pop-in events are often caused by the rupture of the film and/or of the film/substrate interface. In order

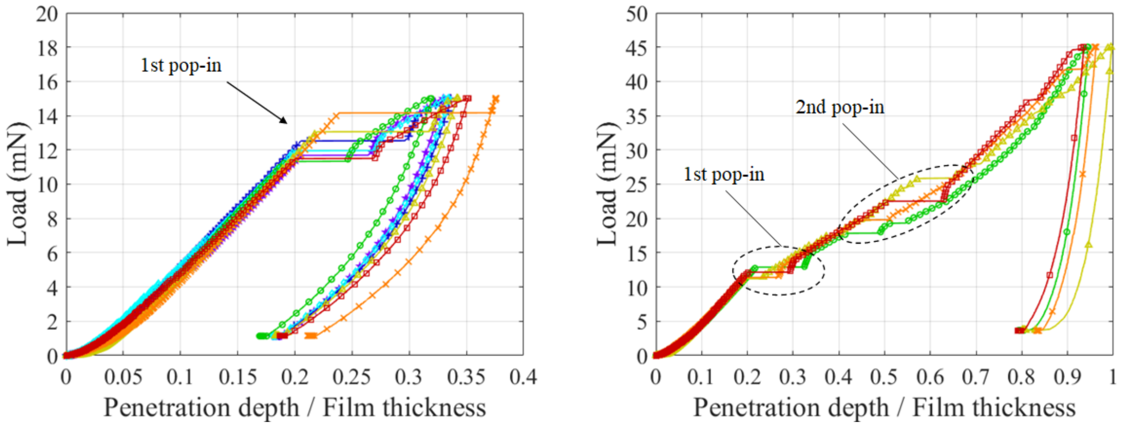

(a) (b)

Figure 2: Representative experimental nanoindentation curves revealing large pop-in events. (a) Maximum load = 15 mN. (b) Maximum load = 45 mN.

to identify which cracking mechanism occurred, *post mortem* images of indented zones were taken: Fig. 3.a and 3.b present representative SEM top-views of zones indented with maximum loads of 15 mN and 45 mN, respectively. Fig. 3.a shows that no signature of the indent can be observed for tests performed at 15 mN. On the contrary, a complex residual imprint is observed after 45 mN tests (Fig. 3.b): a central hole is surrounded by peripheral cracks. A cross-section of this imprint has then been obtained by FIB-milling along the dotted line. On this cross-section view, damage of the Si_3N_4 film by cracking is clearly revealed. The cracks, that display a concentric distribution centered on the indentation axis, can be classified into two types:

- ① cracks between the $Si_3N_4/AlSiCu$ interface and the tip apex imprint. Located at about $1.0 - 1.5$ μm from the indentation axis at the $Si_3N_4/AlSiCu$ interface, they converge towards the tip apex imprint without emerging at the film surface;
- ② orthoradial cracks visible on the film surface and extending into the film thickness with a 'comma-shape'.

In the following, the objective of the study is first to identify by FEM modelling the origin of the two pop-ins observed on the nanoindentation curves and to relate them to the cracks observed on the cross-section view. More generally, this study aims at defining a methodology to determine the damage properties of a $'brittle - film - on - ductile - substrate'$ from the experimental loading curves only.

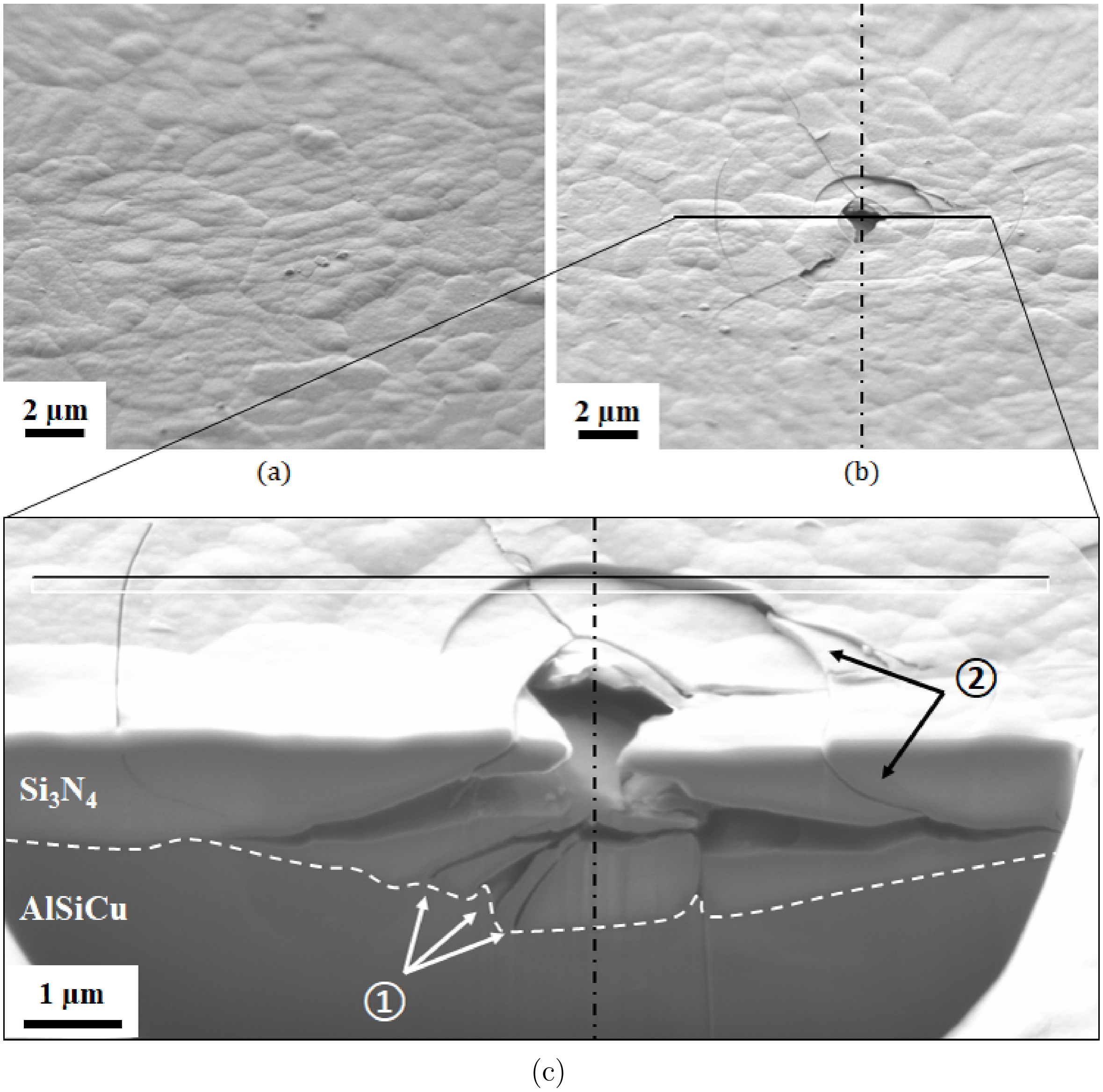

Figure 3: SEM views of residual imprints of indents corresponding to the loading curves of Fig. 2. (a) Top-view after an indent up to 15 mN. (b) Top-view after an indent up to 45 mN. (c) Cross-section view after FIB-slicing of imprint of Fig. 3.b.

4. FEM modelling of cracking under nanoindentation

4.1. Global presentation of the FEM model

The mechanical model is set up in a 2D axisymmetric framework. It consists of one ‘indenter’ brought into contact with the ‘sample’ by a prescribed displacement applied to the indenter (the model is depicted in Fig. 4). With this approach, the nanoindentation tests are performed in a *displacement-controlled* mode. The indenter is modelled as an analytical rigid body. Its conico-spherical profile is designed to fit the area shape function $A(h)$ of a Berkovich indenter (where $A(h)$ is the indenter section at a distance h from the tip apex). The opening angle of the indenter is 70.32 ° .

The sample is modelled as a stack of three layers and a substrate which are (from top to bottom in Fig. 4):

- A 1.3 μm thick Si_3N_4 layer, with an isotropic linear elastic behavior.
- A 3 μm thick $AlSiCu$ layer, elastic-plastic. It is assumed to be linear isotropic in the elastic regime. In the plastic regime, an isotropic hardening is assumed, following a Hollomon type power law:

  $$\sigma_y = \sigma_{y0} + k(\epsilon_p^{eq})^n \tag{1}$$

  where σ_y is the yield stress, ϵ_p^{eq} the equivalent plastic strain, k and n two constants. Note that σ_{y0}, k and n have been identified from experimental data, as described in the following.
- A 0.5 μm thick SiO_2 layer, with an isotropic linear elastic behavior.
- A 6 μm thick Si substrate, with a linear isotropic elastic behavior.

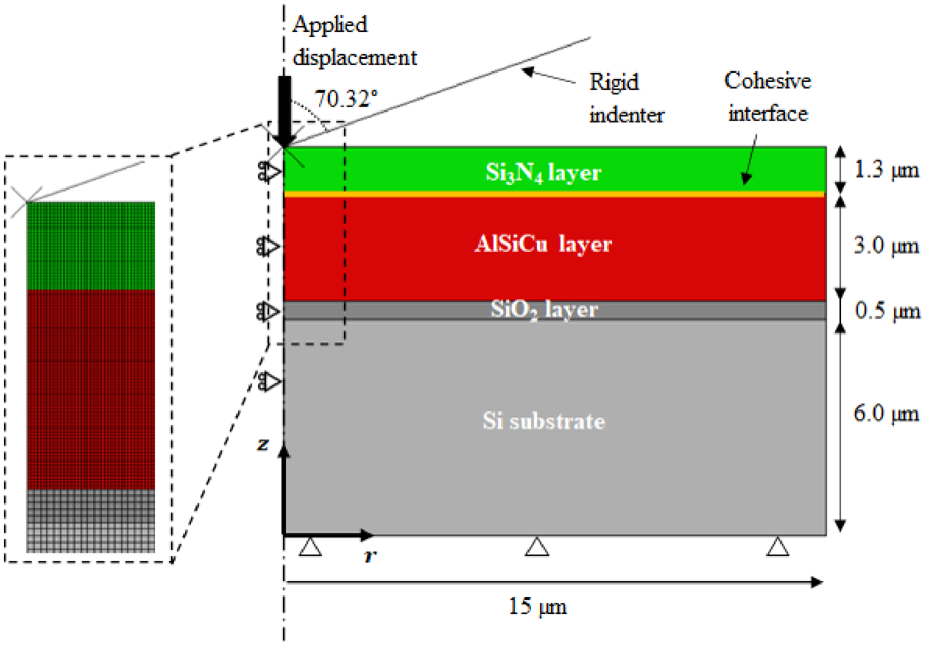

Figure 4: Model for the FEM calculations of cracking under nanoindentation.

Note that the simulation cell has been taken wide enough so that the stress/strain fields created inside the sample during indentation do not interact with the outer boundary (global radius of 15 μm taken, as reported in Fig. 4). Moreover it has been checked that taking a thickness of 6 μm for the Si wafer in the computation cell was sufficient (due to the high rigidity of this substrate).

4.2. Structure cracking: cohesive zone modelling

In addition to elastic and plastic material behaviors, crack initiation and propagation have been accounted in the calculations, both inside the Si_3N_4 layer and at the $Si_3N_4/AlSiCu$ interface. The fracture has been described using a cohesive zone model (e.g. among many others: Tvergaard and Hutchinson (1992); Xu and Needleman (1993)).

The cohesive behavior of cracks is characterized in our case by an irreversible bilinear softening model (Fig. 5): when opposite crack faces in the cohesive zone undergo relative *normal* displacement δ_n , a *normal* traction $T_n = K\delta_n$ develops at the interface where K is the stiffness (pure mode I). Given the cohesive traction ${T_n}^0$ and the work of rupture ${G_I}^c$, the displacement at full rupture ${\delta_n}^f$ is defined by ${G_I}^c = 1/2\ T_n^0{\delta_n}^f$. In addition, adhesion irreversibility is modeled by a damage variable d which increases monotonically from 0 to 1 as the maximum interfacial displacement ${\delta_n}^{max}$ increases from ${\delta_n}^0 = {T_n}^0/K$ to ${\delta_n}^f$. Damage affects the cohesive zone by reducing the stiffness by a factor $1-d$ so that $T_n = K(1-d)\delta_n$ which is zero if the surfaces are brought back into contact after full rupture. In this case, simple frictionless unilateral contact applies. A similar model is applied for pure mode II, with work of adhesion ${G_{II}}^c$ and cohesive traction ${T_t}^0$. In our case, the total work of rupture G^c, which is the sum of ${G_I}^c$ and ${G_{II}}^c$, is assumed to be independent of the mode mix (i.e. the dissipated energy associated with full crack opening always takes the value G^c that we prescribe, irrespective of the particular way this opening is performed).

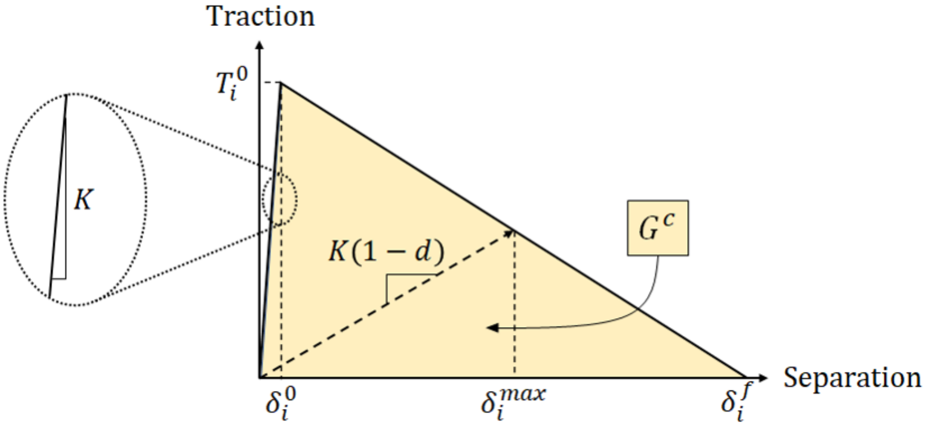

Figure 5: Traction versus separation law for the cohesive zone description of fracture (i= n for mode I and t for mode II).

For the Si_3N_4 layer, as well as for the $Si_3N_4/AlSiCu$ interface, the three material parameters to be defined are T_n^0, T_t^0 and G^c. In the following, these quantities will be denoted $T_n^{0,int}$, $T_t^{0,int}$ and G_c^{int} for the interface and $T_n^{0,lay}$, $T_t^{0,lay}$ and G_c^{lay} for the Si_3N_4 layer.

The finite elements implementation of the above described mechanical model has been carried out with the FEM software ABAQUS®. The crack propagation has been implemented using a Cohesive Zone Model (CZM), within a 'cohesive interaction' framework. Instead of using cohesive elements, this technique uses a contact algorithm including the definition of a cohesive behavior (as defined above). This is hence a surface to surface interaction. The crack initiation criterion that has been chosen for the interface is a quadratic criterion on the traction components:

$$\left(\frac{T_n}{T_n^{0,int}}\right)^2 + \left(\frac{T_t}{T_t^{0,int}}\right)^2 = 1 \tag{2}$$

Regarding the crack in the Si_3N_4 layer, the 'cohesive segments method' implemented in ABAQUS® was used. This approach is developed within the framework of X-FEM, with basis of classical shape functions is enriched with the Heaviside step function across the crack surface[1]. The crack opening follows the cohesive traction-separation law described above. In this case, the maximum principal stress criterion was chosen for crack initiation:

$$\frac{< \sigma_{max} >}{\sigma^{0,lay}} = 1 \tag{3}$$

The $< . >$ symbol means that the crack is only triggered if σ_{max} is positive (tensile stress). The main advantage of this method is that the crack path does not have to be defined in advance. Indeed, once the maximum principal stress criterion is reached within an element, a crack is initiated in the direction *normal* to the maximum tensile stress direction. Note that in this case, $\sigma^{0,lay}$ is actually introduced as a material parameter, whereas $T_n^{0,lay}$ and $T_t^{0,lay}$ are subsequently computed at the increment when the criterion is met.

This crack description allows both crack initiation and propagation. We will however sometimes define an initial location of an enriched feature to study the influence of crack location.

The problem contains four sources of non-linearities: 1) in geometry, due to large deformations (particularly underneath the indenter), 2) in the $AlSiCu$ material behaviour due to plasticity, 3) for the contact developing between the indenter and the surface of the Si_3N_4 layer and 4) due to the loading path dependent crack propagation. Due to this strong non-linear nature of the problem, an implicit dynamic time

---

[1] Note that there are no elastic asymptotic crack-tip functions in this case.

integration procedure is used to calculate the quasi-static response of the system, using the ABAQUS®/standard solver. A Hilber-Hughes-Taylor time integration procedure is carried out (an extension of the Newmark β-method). The Hilber-Hughes-Taylor operator is implicit. The set of simultaneous non-linear dynamic equilibrium equations are solved iteratively using Newton's method. Finally the elements used are 4-node bilinear, reduced integration with hourglass control (CAX4R in ABAQUS®), possibly enriched in the Si_3N_4 layer to model cracks, as discussed above. Elements size in the Si_3N_4 and $AlSiCu$ layers is set at $50\ nm$.

Material	Si_3N_4	$AlSiCu$	SiO_2	Si	Unit
Elastic Behavior	$E_1 = 160$	$E_2 = 50$	$E_3 = 68$	$E_4 = 165$	GPa
	$\nu_1 = 0.27$	$\nu_2 = 0.3$	$\nu_3 = 0.17$	$\nu_4 = 0.22$	–
Plastic Behavior	None	$\sigma_{y0} = 61.8$	None	None	MPa
		$k = 113$			MPa
		$n = 0.09$			–
Cohesive Behavior	$\sigma^{0,lay} = 2.5$	None	None	None	GPa
	$G_c^{lay} = 1$				J/m^2

Table 1: Material properties used in FEM simulations.

4.3. Identification of the parameters for AlSiCu plasticity

In order to access the $AlSiCu$ mechanical properties, nanoindentation tests were performed directly on the $AlSiCu$ film after removal of the Si_3N_4 film. A typical experimental loading curve is reported in Fig. 6.a. The $AlSiCu$ behavior has been identified on this experimental curve. The system without the Si_3N_4 has been modelled similarly to the method presented in section 4.2. A schematic is depicted in Fig. 7. The plastic behavior of the $AlSiCu$ film is described by a Hollomon-type power law expression, as specified in the previous subsection (see Eq. 1). Three scalar parameters (σ_{y0}, k and n) have to be identified in order to accurately model the material work-hardening. To do so, loading curves are obtained from FEM numerical simulations, and compared to the experimental curve (Fig. 6.a). The loading and boundary conditions used in these calculations are quite similar to those described in Fig. 4, except that there is no Si_3N_4 top layer, hence no crack modelling. The three hardening parameters have been obtained using the least-squares method to minimize the summed square of residuals, defined as the difference between the experimental and simulation load-displacement curves as described in Mercier et al. (2017). Those parameters are provided in Tab. 1.

In addition, it has been checked that the contact area between the nanoindentation tip and the $AlSiCu$ layer is consistent between experimental and numerical data (Fig. 6.b).

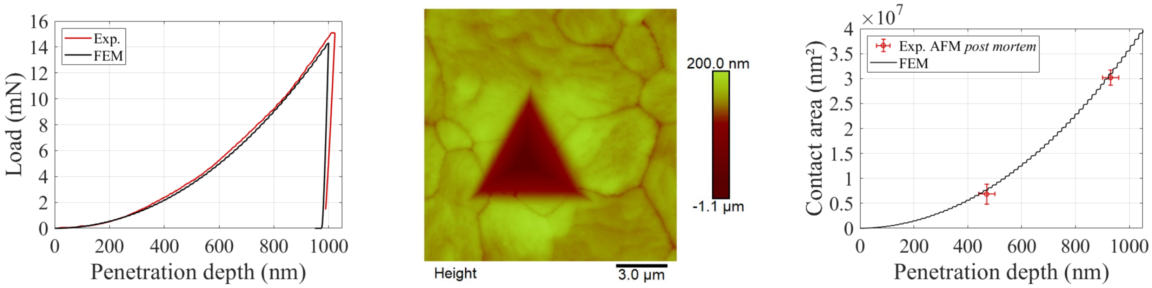

(a) (b) (c)

Figure 6: (a) Load versus displacement curve for a nanoindentation test carried out on the $AlSiCu/SiO2/Si$ stack (comparison between experimental and numerical data for the best fit). (b) AFM topography of a residual imprint after a 1 μm-deep indentation test, the scan size is 15 $\mu m \times 15$ μm (512 × 512 *pixels*). (c) Verification of the good agreement between the experimental contact area measured *post mortem* by AFM and the numerical contact area.

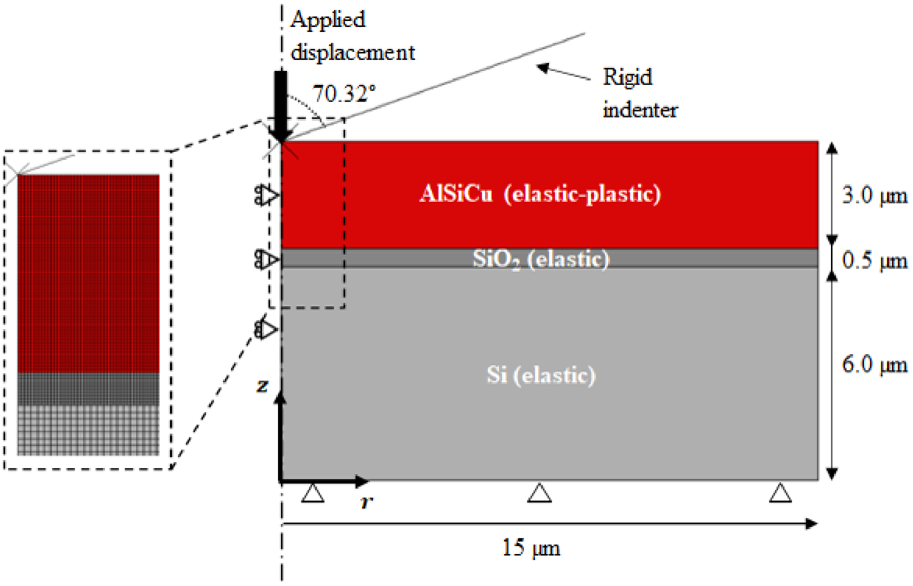

Figure 7: FEM calculation cell used for $AlSiCu$ plastic behavior identification.

5. Simulation of the first pop-in

In this section, the methodology used for the pop-in simulation is described. Such pop-in events during the indentation of $'brittle-layers-on-ductile-substrates'$ have been widely reported, for example in Fu et al. (2013), Fu et al. (2016) and Lofaj and Németh (2017), with some mechanical analysis carried out by FEM (with the use of X-FEM in Lofaj and Németh (2017)). The experimental observations and FE results of these studies focused in cracks occurring outside the contact edge of the indenter, caused by high tensile radial stress on film surface. The value and position of the maximum tensile stress was shown to be affected by the size of the plastic zone in the substrate beneath the indenter. However, the mechanism of a first crack triggering underneath the indenter (not visible from the sample surface), responsible of the first pop-in, has not been described[2]. We will demonstrate that it is the case in our $'brittle-on-ductile'$ system, and that in the process of quantitatively describing the pop-in event on the loading curve, it is possible to obtain an estimate of the tensile strength parameters of the Si_3N_4 layer.

In metals and ceramics, the opening at complete separation (previously denoted δ^f in section 4.2) is known to be of the order of nanometers, and the peak traction values (previously denoted T^0) are ranging between a few hundreds of MPa to a few GPa (Needleman (1987); Yamakov et al. (2006); Leterrier et al. (1997)). By using the FEM simulations and comparing their results to the experimental data, it is possible to narrow down these values.

5.1. Overall stress distribution

First, it is worth analyzing the results of a FEM calculation simulating the indentation of the whole system, without accounting for fracture, in order to have an idea of the stress distribution into the system as the indenter is progressively driven down into the sample. In this context, the distribution of the maximal principal stress component inside the system is plotted in Fig. 8 for an indentation depth $h = 300\ nm$, which is the depth for which the pop-in event is experimentally detected (Fig. 2). The maximum tension area appears in light grey, above the $Si_3N_4/AlSiCu$ interface, and extends up to $1300\ nm$ away from the axis. A lower tensile stress threshold of $3\ GPa$ has been arbitrarily fixed for this grey area, for the sake of representation. Admitting that the pop-in event is associated to the propagation of a crack, we can assume that this crack is initiated inside this grey region. Moreover, since there is no visible sign of crack propagation on the experimental loading curve prior to this loading threshold, it may be assumed that the crack nucleates and propagates for this loading. That provides an estimate of the peak mode I traction, $\sigma^{0,lay}$ around $3\ GPa$ that should be applied to the cohesive behavior of the Si_3N_4 layer. In addition, in the same way that a correct value of $\sigma^{0,lay}$ should be clearly identified in order to match the critical load L_c for which the horizontal pop-in plateau is observed, the length of this plateau should depend on G_c^{lay}, the toughness of the Si_3N_4 layer. Finally, a set of ($\sigma^{0,lay}$; G_c^{lay}) should be chosen in order to reproduce in the closest way the experimental loading curve. It is worth noting the presence of a compression dominated area just underneath the indenter apex (dark grey area in Fig. 8).

5.2. Procedure to model the first pop-in event

The domain of maximal tension where the cracks nucleate and propagate has been identified (light grey area in Fig. 8). Although cracks are likely to nucleate wherever in

---

[2] It is however observed in Lofaj and Németh (2017) that an area of strong maximum tensile stresses is located at the coating/substrate interface under the indenter.

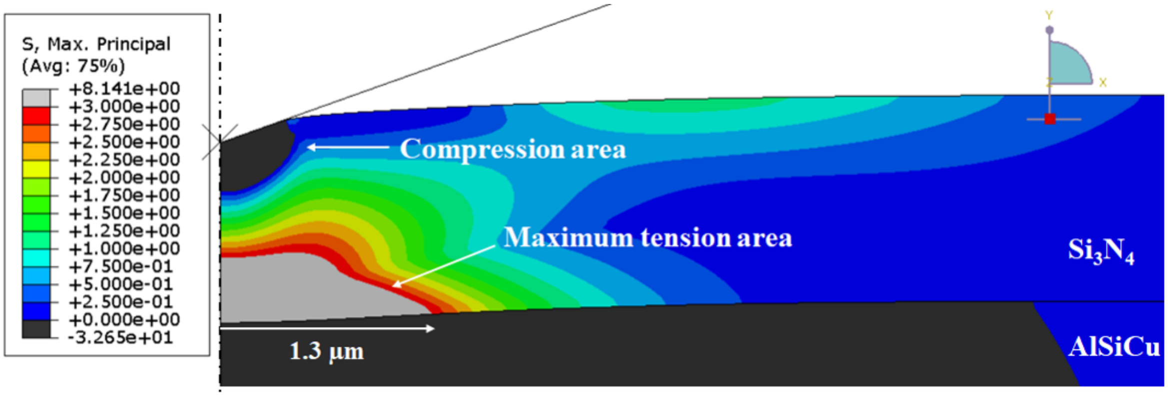

Figure 8: Distribution of the maximal principal stress component (in GPa) inside the system, for an elastic Si_3N_4 layer and an elastic-plastic $AlSiCu$ layer (without crack or delamination). Results were obtained for an indentation depth $h = 300\ nm$ (for which a pop-in event is experimentally detected). Grey area indicates the maximum tension area.

this domain, we assume that it exists a location within this area where a crack is more likely to nucleate. We will denote by r_f the optimal location of this crack (distance of the crack to the axis). In the following, the procedure used to obtain r_f will be presented, and a justification of the existence of such a crack for which propagation is favored will be provided.

In order to determine values of r_f and to show its dependence on the material properties, several simulations were carried out. For each set of simulations, the material data describing the fracture properties ($\sigma^{0,lay}$ and G_c^{lay}) were fixed. As delamination of the $Si_3N_4/AlSiCu$ interface was also allowed, the interface cohesive parameters $T_n^{0,int}$, $T_t^{0,int}$ and G_c^{int} were also kept identical for all the simulations[3]. In each simulation, an initiation site is introduced at a distance r_{ini} of the axis, under the form of a $100\ nm$ long enriched feature (i.e. already initiated crack). This feature is long enough to cross two elements but small compared to the layer thickness ($1300\ nm$). This initial crack, vertical just above the interface, is depicted in Fig. 9.

5.3. Structure cracking for different initiation site locations

A set of simulations with fixed material properties and with varying locations of the initiation site is provided in Fig. 10. On the left side, the state of the system for a penetration depth of $h = 400\ nm$ (depth at which the first experimental pop-in ends) is shown for various values of r_{ini} (increasing from top to bottom). It is clear that the crack propagates quite differently for different r_{ini}. The crack inside the Si_3N_4 layer is visible, as well as some delamination of the interface in the vicinity of the crack. On the right side of Fig. 10, the energy dissipated in fracture is represented as a function of the

---

[3] The choice of the interface parameters will be explained and justified in the following.

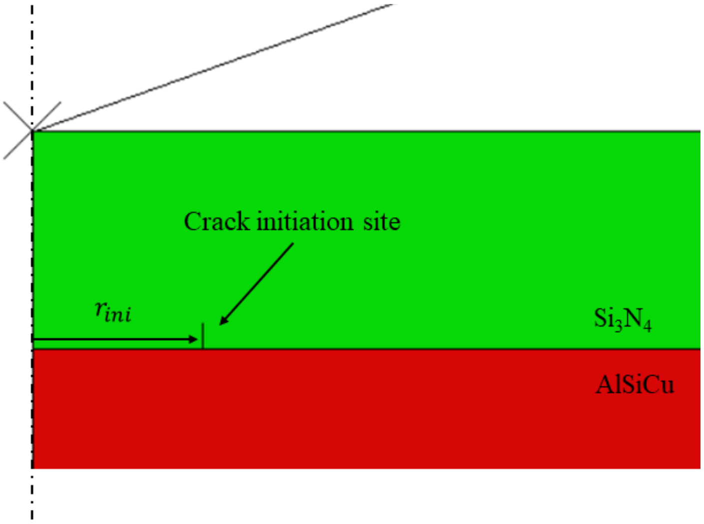

Figure 9: Example of crack initiation site (at r_{ini}) introduced for the calculation of the optimal crack propagation location.

penetration depth normalized to the film thickness h/t, as well as the corresponding loading curve.

For an initiation site far from the axis (Fig. 10.d), no propagation is observed and no pop-in is visible on the loading curve. For smaller distances, as in Fig. 10.a and Fig. 10.b, although crack propagation is observed, no pop-in is visible in the loading curve either. In these three cases, crack propagation dissipates only a small amount of energy. On the contrary, for an initiation site at intermediate location, the effect of crack propagation is clearly visible on the loading curve (right side of Fig. 10.c), as a double elbow feature which is the signature of a *snap-through* instability (detailed below). In this configuration, a large amount of energy is seen to be dissipated by the cracking event.

In terms of crack travel, whatever the initiation site location, if the crack initiates (Fig. 10.a, 10.b and 10.c), it propagates towards the indenter apex. By comparing these figures to Fig. 8, it can be seen that the crack actually stops when reaching the compression zone underneath the indenter apex. Finally, it is to be noted that some interface damage is visible at the vicinity of the crack when it propagates. However, it will be later shown that the interface damage has very little influence on the load versus penetration depth response of the system.

5.4. Snap-through instability

As already stated, the double elbow feature observed in Fig. 10.c is the signature of a *snap-through* instability. Given that the loading in the numerical simulation is performed in a *displacement-controlled* mode, the force decrease at the elbow feature simply indicates that a significant loss of stiffness of the system is associated to the crack propagation. So, as the indenter is pushed deeper into the sample, the reaction force first decreases, then increases again, and the mechanical equilibrium is maintained at every step of the loading. However, in the experiment, the load is imposed in a monotonically increasing way on the indenter (*load-controlled* mode). In this context, when the upper point of the first elbow is reached (point A in Fig. 10.c), a displacement jump is observed on the loading curve, as the next equilibrium point that is accessible for a slightly larger force is point B. This is the origin of the pop-in observed in the experimental data.

5.5. Mapping of crack parameters

In practice, the actual crack location is assumed to be at the distance $r_{ini} = r_f$ that maximizes the energy dissipation. According to Fig. 10, it is possible to identify this critical value of r_{ini} for each value of $\sigma^{0,lay}$. Even though this critical value r_f is *a priori* a function of $\sigma^{0,lay}$ and G_c^{lay}, the influence of G_c^{lay} is rather small (as discussed later). A map of the dissipated energy during crack propagation in a $(r_{ini}\ ;\ \sigma^{0,lay})$ space is displayed in Fig. 11, with a value of G_c^{lay} fixed to $1\ J/m^2$. The distance of the crack to the axis is represented on the horizontal axis, and the layer tensile strength $\sigma^{0,lay}$ on the vertical axis. The red front characterizes the maximum dissipation. For each value of $\sigma^{0,lay}$, a critical value r_f can then be identified. For instance, as seen in Fig. 10, the maximum dissipation at $\sigma^{0,lay} = 3\ GPa$ is obtained for the configuration depicted in Fig. 10.c, at $r_{ini} = 1\ \mu m$. Consequently, Fig. 11 becomes an universal map to relate the material properties to the crack location.

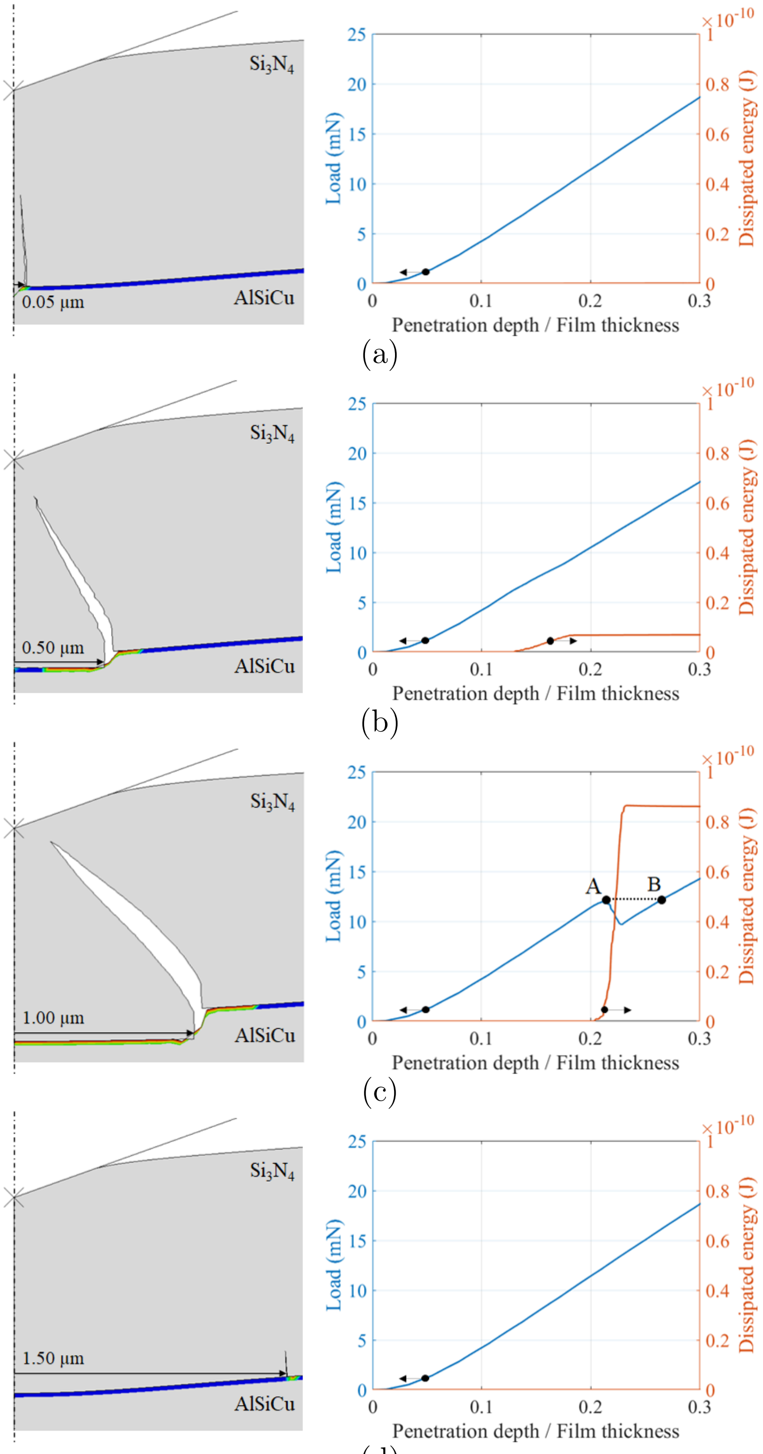

(a)

(b)

(c)

(d)

Figure 10: Simulations results of crack propagation in Si_3N_4, for cracks nucleation sites at various distances from the axis. (a) $r_{ini} = 0.05\ \mu m$, (b) $r_{ini} = 0.50\ \mu m$, (c) $r_{ini} = 1.00\ \mu m$, (d) $r_{ini} = 1.50\ \mu m$. Left: crack as observed for an indentation depth $h = 400\ nm$. Contour plots show the damage parameter of the $Si_3N_4/AlSiCu$ interface ($d = 0$ in blue and $d = 1$ in red). Right: plot of the energy dissipation and reaction force on the indenter as a function of h/t during indentation. The damage properties are fixed: $\sigma^{0,lay} = 3\ GPa$, $G_c^{lay} = 1\ J/m^2$, $\sigma^{0,int} = 100\ MPa$, $G_c^{int} = 1\ J/m^2$.

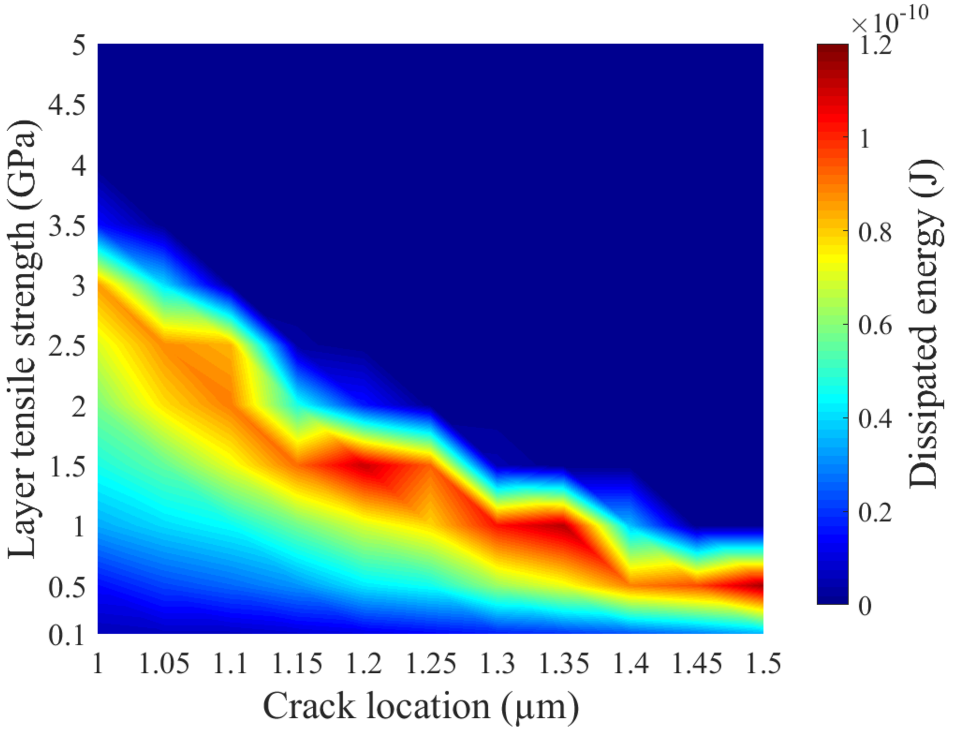

Figure 11: Map of the dissipated energy during the propagation of the 'first' crack (the one propagating in the area underneath the indenter). Horizontally: distance of the crack to the axis; Vertically: layer tensile strength $\sigma^{0,lay}$. This map gathers the results of 121 simulations, with horizontal and vertical grid steps of 50 nm and 0.5 GPa, respectively.

6. Analysis of the first pop-in event

6.1. Tensile strength values of Si_3N_4 obtained from the first pop-in

As the pop-in events observed on the experimental loading curves can be well represented using our FEM numerical simulations, we now want to use the pop-in characteristics as a signature to identify the cohesive parameters of the Si_3N_4 layer. The procedure is based on an inverse method, similar to the one that was used to identify the hardening properties of $AlSiCu$, previously described in section 4.3. The identification procedure is based on:

- the critical loading state for which the plateau is reached, formed by the couple $(h_c\ ;\ L_c)$, respectively the critical depth and critical load at which the pop-in occurs;
- the length of the plateau itself, further denoted Δh_c.

A set of experimental loading curves (out of a matrix of 12 indents) are displayed in Fig. 12.a. A relatively good reproducibility can be observed regarding the load at the pop-in plateau, as well as the length of this plateau.

The loading curves obtained numerically with six sets of $(\sigma^{0,lay}\ ;\ r_f)$ data allowing the maximum energy dissipation (see section 5.5) are displayed in Fig. 12.b. The average and standard deviation values of both load and depth observed experimentally have also been represented in Fig. 12.b. It is seen that all the couples lying between $(3.0\ GPa\ ;\ 1.00\ \mu m)$ and $(0.5\ GPa\ ;\ 1.50\ \mu m)$ generate loading curves falling withing the range of experimental output. A curve obtained from the FEM showing values of L_c and Δh_c within the experimental range is also reported in Fig. 12.a and compared to the set of experimental curves. As discussed before, the double elbow shape of the loading curves obtained experimentally characterizes the $snap - through$ instability that is triggered at the opening of the crack (sudden decrease of stiffness of the system) which implies a jump on the experimental curve because of the monotonic increase of the experimental loading. In order to narrow down the interval of tensile fracture strength values $\sigma^{0,lay}$ identified from the simulation, the second pop-in must also be exploited.

6.2. Influence of G_c^{lay}

So far, only the influence of $\sigma^{0,lay}$ on Δh_c and L_c has been considered through a parametric approach. The role of G_c^{lay} needs to be assessed. To do so, the loading curves obtained numerically for 3 sets of $\sigma^{0,lay}, G_c^{lay}$ values matching the same pop-in plateau $L_c = 12\ mN$ have been reported in Fig. 13. The values of G_c^{lay} vary in a ratio of 1000, while the tensile strength values $\sigma^{0,lay}$ only vary in a ratio of 1.4. A similar double elbow feature is observed on all curves. Changing G_c^{lay} does not affect the pop-in initial and ending points, thus showing the lesser role of G_c^{lay}. This indicates a fracture

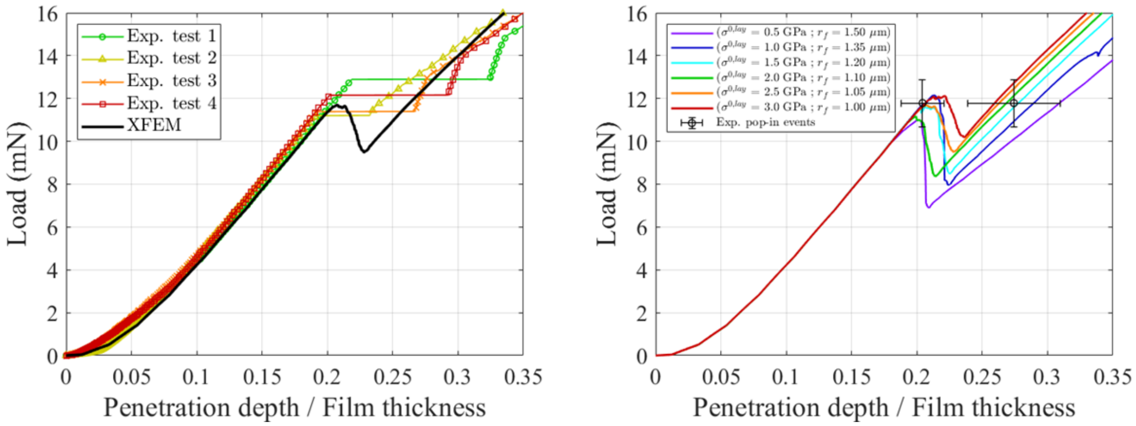

(a) (b)

Figure 12: Loading curves versus penetration depth. (a) The experimental data from various indents are gathered. One of the best fit FEM simulations results is plotted (black curve with double elbow) with $\sigma^{0,lay} = 2.5\ GPa$ and $r_f = 1.05\ \mu m$. (b) Sets of $(\sigma^{0,lay}\ ;\ r_f)$ data providing loading curves within the experimental data range (experimental error bars indicated).

mechanism that is essentially stress controlled in the sense that, once the initiation criterion is met, the crack is be able to propagate over a long distance due to a large energy release rate. It only stops when the crack fronts enter a compression dominated area (i.e. just underneath the indenter).

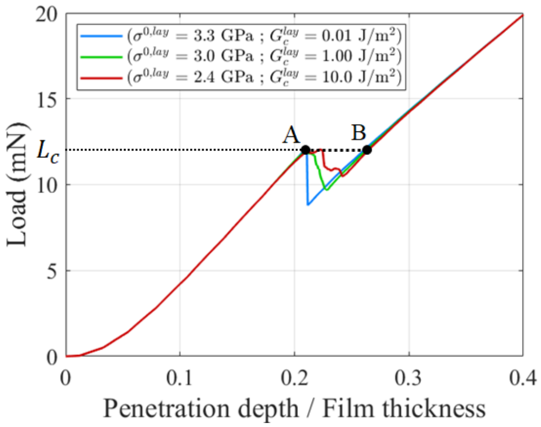

Figure 13: Influence of the two layer parameters $\sigma^{0,lay}$ and G_c^{lay} on the value of the pop-in load plateau L_c. The values of $\sigma^{0,lay}$ necessary to trigger the pop-in at this value of L_c show little variation as G_c is varied of a thousand-fold (for $r_{ini} = 1\ \mu m$).

6.3. Cohesive behavior of the interface

At this point, it is necessary to discuss the choice of the parameter values for the interface cohesive behavior. These parameters have been previously introduced: the peak traction components in the normal and tangential direction (respectively $T_n^{0,int}$ and $T_t^{0,int}$) and the adhesion energy G_c^{int}. Because the crack in Si_3N_4 is connected to the interface, a shear loading develops at the interface in the vicinity of the crack. Hence, the shear traction component ($T_t^{0,int}$) is the dominant parameter for the initiation of interface delamination. Regarding the value of the shear strength at a ceramic coating/metal interface, values of the order of a hundred MPa can be found (Shieu and Shiao (1997); Nieva et al. (2012)). However, the experimental values for G_c^{int} found in the literature must be interpreted with care. Indeed, the energy measured experimentally during interface separation often involves a significant amount of plastic work in the metal, that is not to be implemented as interface adhesion energy in the simulation parameters. Calculations of adhesion at metal/ceramic interfaces based on first principle calculations estimate G_c^{int} around about 1 J/m^2 (Alemany et al. (1993); Jiang et al. (2010)) or even less.

A range of interface property values have been tested in the FEM calculations, with $T_t^{0,int} \in [100, 500]$ MPa[4] and $G_c^{int} \in [0.01, 10]$ J/m^2 (Appendix). It has been observed that for $T_t^{0,int} < 200$ MPa, a part of the interface delaminates by shear in the vicinity of the crack, whereas for $T_t^{0,int} > 200$ MPa the interface remains unbroken.

The main information resulting from the parametric study concerning the interface is that the pop-in response identified on the loading curve is not affected by the various interface damage scenarios (see Fig. 17 in Appendix). This indicates that it is not possible to collect informations about interfacial fracture properties from the indentation test as it is carried out in this study. However, it also simplifies the identification of the tensile strength of the Si_3N_4 layer.

Finally it is possible to narrow down the interval of values of the ($\sigma^{0,lay}$; r_f) couples, in order to obtain more precisely the strength of the Si_3N_4 layer. This is possible using the experimental data from the second pop-in, as will be now explained.

7. Study of the second pop-in event

In this section, the mechanical study of the second pop-in event is carried out. A FEM calculation has been performed for each couple of ($\sigma^{0,lay}$; r_f) satisfying the maximum energy dissipation and providing results consistent with the experiments (see Fig. 12.b). For these tests, the loading was pursued further after the first pop-in event (up to 900 nm depth). It is worth noting that, in addition to the first crack responsible for the first pop-in, cracks are also allowed to nucleate and propagate anywhere else in the layer. Finally the interface strength and toughness parameters have been fixed to 100 MPa and 1 J/m^2 respectively, consistently with data from the literature[5].

---

[4] The peak value for the normal traction, $T_n^{0,int}$, has been set to the same value as $T_t^{0,int}$. This has no incidence on the results as the traction is clearly shear dominated in the decohesion area.

[5] It is recalled that those interface parameters have been demonstrated not to influence the loading curve response.

The numerical results are displayed Fig. 14, as well as the experimental data scattering (black crosses). First, it can be seen that the experimental characteristics of the second pop-in (pop-in plateau load L_{c2} and displacement jump Δh_2) are much more scattered than it is the case for the first pop-in. Interestingly, on the contrary to the first pop-in, the second pop-in is *very dependent on the chosen* $(\sigma^{0,lay}\ ;\ r_f)$ couple. The data $(\sigma^{0,lay}\ ;\ r_f)$ which are valid are those for which the simulated second pop-in plateau lies within the experimental scattering interval (level of pop-in load). Thus it becomes possible to identify the relevant range for these magnitudes. In the present case, from the data represented in Fig. 14, it can be concluded that $2.0\ GPa \leq \sigma^{0,lay} \leq 3.0\ GPa$ and $1.0\ \mu m \leq r_f \leq 1.1\ \mu m$.

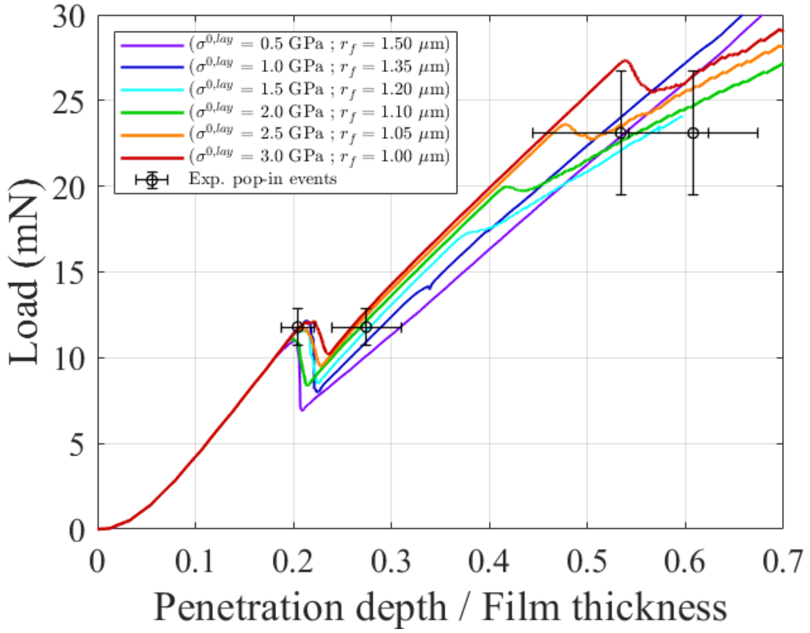

Figure 14: FEM simulated loading curves are reported for couples of $(\sigma^{0,lay}\ ;\ r_f)$ data allowing maximum dissipation for the first crack. The scattering of experimental data is also reported (black crosses).

It is worth discussing the sensitivity of our results to materials parameters, and the possible role of uncertainties, whether they are 'epistemic' (i.e. possible to be reduced by gathering additional data or refining the model) or 'aleatory' (i.e. no possibility is seen of reducing them) (Der Kiureghian and Ditlevsen, 2009; Castaldo et al., 2019). Up to this point, our approach has been rather focused on the understanding of the failure mode and the measure of the layer strength, but the latter is likely to be affected by aleatory uncertainties related to local heterogeneities (small-scale defects, interface coherences, ...). As already discussed, in terms of experimental characteristics, the first pop-in displays a very small experimental dispersion (Fig. 2.a) while the second pop-in presents much more scattered features (Fig. 2.b). In terms of numerical results, the impact of these two cracks on the loading curve is also drastically different: for the first pop-in, the locus of the fitting parameters that maximize the energy release (very sharp and stretched area in Fig. 11) shows that the description of this first crack is highly sensitive to numerical inputs (small changes in numerical strength or crack location induce a large deviation in dissipated energy) even though a wide range of ($\sigma^{0,lay}$; r_f) couples can fairly describe it. This latter point actually prevents the direct identification of the actual layer characteristics solely from the first pop-in. On the contrary, for the second pop-in, despite the dispersed experimental characteristics, only a limited range of numerical inputs allow the overall description of the experimental results.

As the presence of defects can influence the location of crack nucleation, a sensitivity study of the problem regarding the location of cracks has been carried out. The variations of dissipated energy with respect to the crack locations are reported in Fig. 15.a. For all the simulations, the strength $\sigma^{0,lay}$ is fixed to 2.5 GPa, for which the optimal crack locations (i.e. associated with the highest release of energy) are $r_1^* = 1.05$ μm and $r_2^* = 3.9$ μm for the first and second crack, respectively. The corresponding released energies are denoted E^* and E (positive values) for the optimal and tested crack locations, respectively. The quantities plotted in Fig. 15.a are relative to the optimal parameters: $(E - E^*)/E^*$ as a function of $(r - r_1^*)/r_1^*$ (first crack) or $(r - r_2^*)/r_2^*$ (second crack). The variation of the energy release with respect to the first crack location shows a sharp peak at the optimal value, so the system is not expected to deviate much from this value, whatever the distribution of structural defects within the material. This point explains the small dispersion on the first pop-in features. On the contrary, the variation of the energy release with respect to the second crack location is quite weak, with a 5 % variation in energy over a 45 % range of crack location span. So the location of the second crack is more likely to be sensitive to structural defects. To further understand the nucleation process of this second crack, the numerically computed distribution of maximum principal tensile stress component in the Si_3N_4 layer just before crack initiation has been plotted versus crack location (Fig. 15.b). It appears that the stress value does not decrease quickly in the vicinity of the peak, in fact it only varies from 5 % over a 1 micrometer span from the peak. Of course, in calculations the crack forms at the peak value of the stress. However, this is where the ‘aleatory’ defects in the ‘real’ layer may take a part, as the weakest defects may trigger cracks not exactly at the numerically-predicted location, but rather in a close vicinity of this stress peak. This finally sheds light on the experimental dispersion on the loading curve for the second pop-in, as both tensile stress and released energy vary very weakly over a large region of the film during the phenomenon.

The result of the calculation for $\sigma^{0,lay} = 2.5$ GPa and $r_f = 1.05$ μm is shown Fig. 16.a. It can be seen that a radial crack forms at a distance $r = 3$ μm of the axis, starting

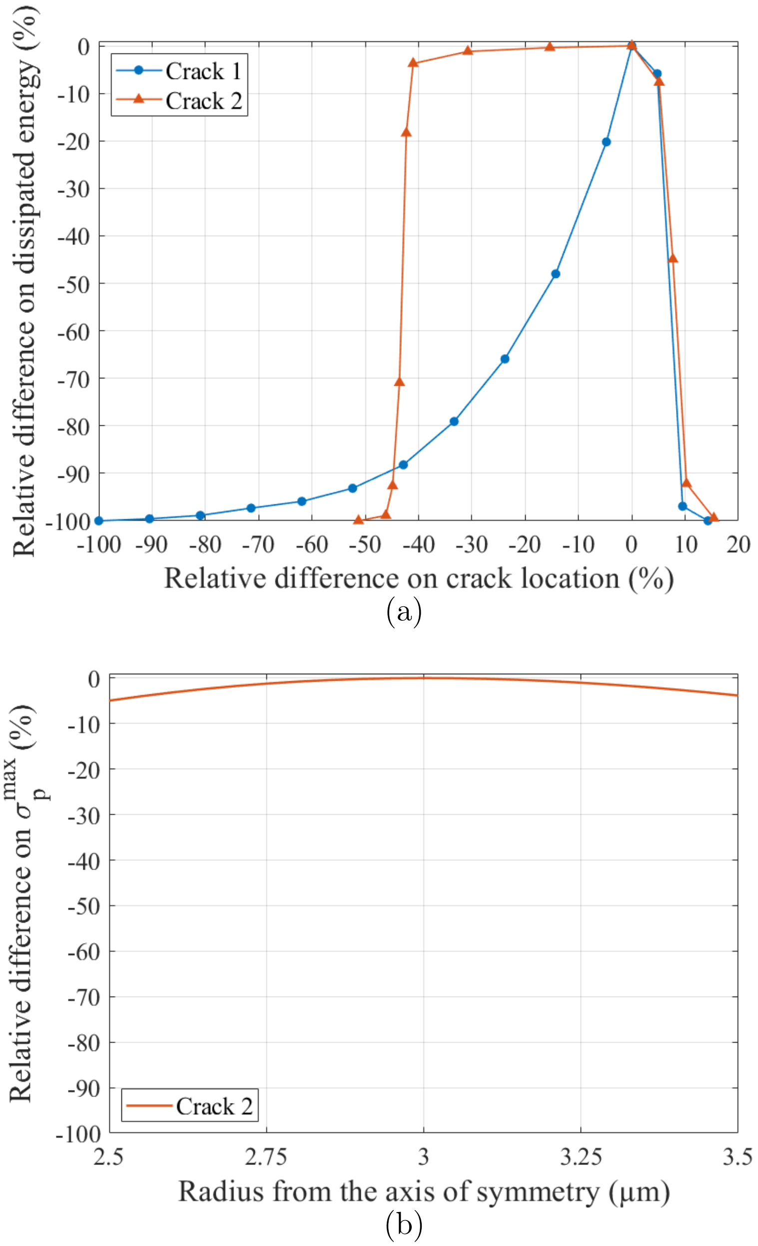

Figure 15: (a) Variations of dissipated energy with respect to crack locations. The quantities plotted are relative to the optimal parameters: $(E - E^*)/E^*$ as a function of $(r - r_1^*)/r_1^*$ (first crack) or $(r - r_2^*)/r_2^*$ (second crack), with optimal values $\sigma^{0,lay} = 2.5\ GPa$, $r_1^* = 1.05\ \mu m$ and $r_2^* = 3.9\ \mu m$. (b) Numerically computed distribution of tensile stress in the Si_3N_4 layer just before the crack initiation (indenter depth $h = 580\ nm$).

from the surface, propagating down into the layer, kinking from an initially vertical to horizontal propagation direction. The simulated loading curve has been reported in Fig. 16.c, together with an experimental curve. A second pop-in event is clearly observed on the FEM obtained curve, associated with the propagation of the second crack. A similar second pop-in feature can be observed on the experimental curve.

As the loading curve only gives information about the global response of the sample, it is worth obtaining complementary data from the direct observation of the fracture pattern. This can be performed on the SEM cross-section obtained after by FIB-milling of a residual imprint (as shown in Fig. 3.b). In order to compare experimental observations to simulation results, this SEM cross-section view is reported again in Fig. 16 with its numerical counterpart. The corresponding pop-ins are recalled on the experimental and numerical loading curves (Fig. 16.c). Remarkably, the two main cracks that have been identified in the simulation as causing the first and the second pop-in events can be observed on the image, at locations that are consistent with the numerics (respectively $\sim 1\ \mu m$ and $\sim 3\ \mu m$ from the axis for the first and the second crack). Likewise, the experimental crack paths were also correctly predicted by simulations: while cracks ① nucleate at the $Si_3N_4/AlSiCu$ interface and propagate up to the indenter apex, cracks ② kink from a vertical to an horizontal direction, going away from the indenter. All these observations confirm the ability of the model to be predictive and bring confidence to the reliability of the data values determined for the Si_3N_4 tensile strength.

8. Conclusion

The formation of multiple cracks during the nanoindentation of a stack composed of a silicon nitride (Si_3N_4) layer deposited on top of a ductile metallic alloy ($AlSiCu$) layer was investigated. The complete damage process of the multilayer during indentation was analyzed using FEM, accounting for plasticity in $AlSiCu$ and crack propagation in the Si_3N_4 layer. The various stages of the damage process occurring in the Si_3N_4 were elucidated, showing in particular:

- The initiation/propagation of a crack of conical shape, nucleating from a location along the interface and propagating towards the apex of the indenter. The crack does not reach the surface, as it is stopped in a compression zone underneath the indenter. It explains why this crack can not be observed on the sample surface. However, observations of a sample cut reveals its presence.
- A second crack initiation and propagation following the first one, but this time propagating from the top surface of the layer down towards the $Si_3N_4/AlSiCu$ interface.

Moreover, a novel procedure for the identification of the Si_3N_4 layer tensile strength is presented, using an inverse method based on FEM simulations and experimental data. The procedure is composed of two steps:

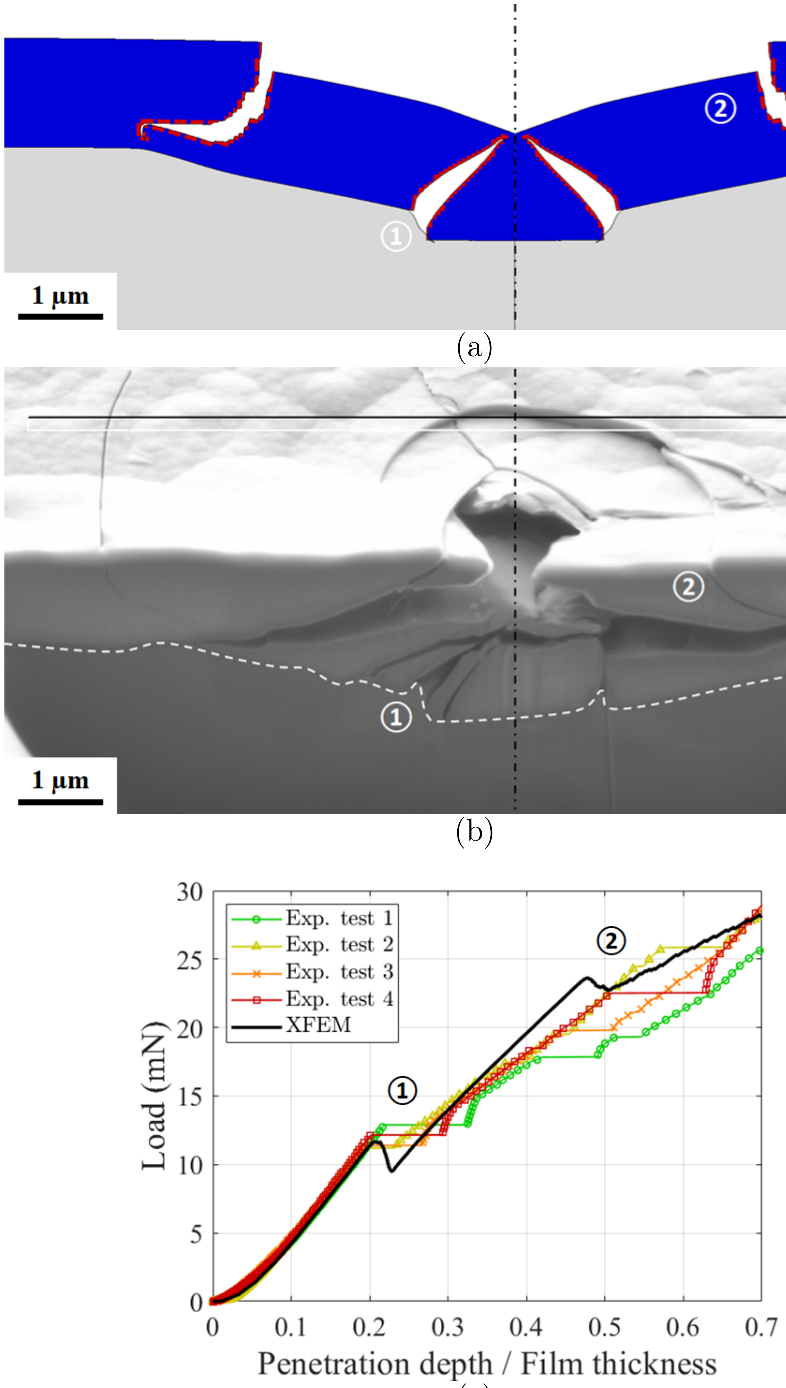

(a)

(b)

(c)

Figure 16: Comparison between the numerically predicted crack pattern (a) and the experimental one (b). The experimental and numerical loading curves are recalled (c). The cracks associated to the first and second pop-in events are labelled, respectively, ① and ②.

- Step 1: Fitting on the first pop-in. Only two physical magnitudes are adjustable parameters for this fitting step: the layer tensile strength $\sigma^{0,lay}$ and the distance of the crack to the indenter axis r_f. A collection of these parameters able to match the first pop-in has been identified as follows: for each value of $\sigma^{0,lay}$, the value of r_f maximising the energy dissipation is selected. It is to be noted that the characteristics of the first pop-in on the experimental loading curves (critical load and depth) are fully reproduced by the numerical curves obtained with this 'maximum energy dissipation' approach.

- Step 2: Fitting on the second pop-in. Within the collection of ($\sigma^{0,lay}$; r_f) couples identified at Step 1, only a limited set of couples are able to reproduce the second pop-in behavior: critical load and depth, snap-through feature, ...

The strength of this two-step procedure relies on its ability to narrow down the identification range for the layer properties. Indeed, at Step 1, all the ($\sigma^{0,lay}$; r_f) couples maximising the energy dissipation result in similar characteristics of the simulated first pop-in (critical load and depth). Consequently, the fitting of this first pop-in is not sufficient to discriminate a tensile strength value by itself. By contrast, the characteristics of the simulated second pop-in are much more sensitive to the ($\sigma^{0,lay}$; r_f) couples, opening a way for a closer identification of the layer property. It is worth noting that the experimental dispersion on this second pop-in is small enough to allow this identification. This implies that a remarkably good estimate of the layer tensile strength can be achieved by the method described here.

Finally, this double pop-in phenomenon is probably very generic to brittle layers deposited on ductile underlayers, and is indeed observed in other works (see e.g. Lofaj and Németh (2017)), but up to now, each pop-in had not been clearly attributed to a first crack forming underneath the indenter before a circumferential crack, probably due to the difficulty that the first crack can not be spotted from surface observations, and is more likely attributed to a circumferential crack. In our case, the FIB observation clearly confirmed the existence of this under-surface crack. Because our modelling approach is very general as it involves only a few influential key parameters to describe fracture and plasticity, the identification procedure that we propose should be quite generic to systems of brittle/ductile layers showing similar multiple-cracking patterns under indentation.

Acknowledgments

This work has been performed with the financial support of the Centre of Excellence of Multifunctional Architectured Materials "CEMAM" n°ANR-10-LABX-44-01. The CEMAM program is funded by the French Agence Nationale de la Recherche (ANR). This study was also supported by the Carnot-ANR Pack5G project, the Normandy region and European Regional Development Fund through the project RIN RECHERCHE PLACENANO Contract No. 18E01664/ 18P02478.
The authors would like to thank F. Charlot for FIB preparation and SEM observations, S. Froissart for SEM observations and C. Pistis for sample preparation.

Appendix 1: Illustration of the weak influence of the interface properties on the load vs penetration depth curve

As the first crack initiates at the interface between Si_3N_4 and $AlSiCu$, it is necessary to consider the possible delamination of this interface during the loading of the system. A wide range of interface shear strength ($\sigma_t^{0,int}$) and toughness (G_c^{int}) have hence been tested numerically. In all cases, there was no influence on the loading curve (the pop-in load was the same), as illustrated in Fig. 17.a. The damage distribution along the interface is also plotted Fig. 17.b. Three cases are observed: 1) for high $\sigma_t^{0,int}$ and moderate G_c^{int}, the interface is damaged only at the crack location, 2) for moderate $\sigma_t^{0,int}$ and moderate G_c^{int}, some interface damage by shear can form between the crack and the axis of symmetry and 3) for moderate $\sigma_t^{0,int}$ and small G_c^{int}, the interface can be damaged by shear on a wide area extending far from the axis of symmetry. This last case is unrealistic though, as it requires a very small value for G_c^{int}.

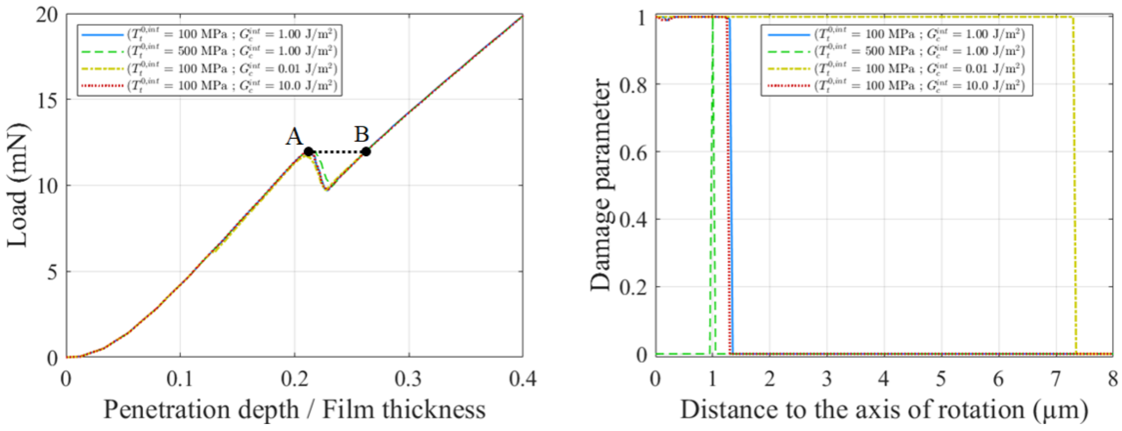

(a) (b)

Figure 17: Influence of the interface strength and toughness on the calculations results. (a) Load versus penetration curve obtained during the simulation of nanoindentation, for a large spectrum of values of the interface shear strength $\sigma_t^{0,int}$ and toughness G_c^{int}. (b) Damage parameter along the interface, for the same sets of interface strength and toughness values.

References

Aberle, A., 2000. Surface passivation of crystalline silicon solar cells: A review. Progress in Photovoltaics 8, 473–487.

Alemany, P., Boorse, R.S., Burlitch, J.M., Hoffmann, R., 1993. Metal-ceramic adhesion: quantum mechanical modeling of transition metal-alumina interfaces. The Journal of physical chemistry 97, 8464–8475.

Beegan, D., Chowdhury, S., Laugier, M., 2004. The nanoindentation behaviour of hard and soft films on silicon substrates. Thin Solid Films 466, 167–174.

Bradby, J.E., Williams, J.S., Wong-Leung, J., Swain, M.V., Munroe, P., 2002. Nanoindentation-induced deformation of ge. Applied Physics Letters 80, 2651–2653.

Bull, S.J., 2005. Nanoindentation of coatings. Journal of Physics D: Applied Physics 38, R393–R413.

Bustillo, J., Howe, R., Muller, R., 1998. Surface micromachining for microelectromechanical systems. PROCEEDINGS OF THE IEEE 86, 1552–1574.

Castaldo, P., Gino, D., Mancini, G., 2019. Safety formats for non-linear finite element analysis of reinforced concrete structures: discussion, comparison and proposals. Engineering Structures 193, 136–153.

Cazako, C., Inal, K., Burr, A., Georgi, F., Cauro, R., 2018. Hypothetic impact of chemical bonding on the moisture resistance of amorphous SixNyHz by plasma-enhanced chemical vapor deposition. Metallurgical Research & Technology 115.

Chen, J., Bull, S., 2006. Assessment of the toughness of thin coatings using nanoindentation under displacement control. THIN SOLID FILMS 494, 1–7. 32nd International Conference on Metallurgical Coatings and Thin Film, San Diego, CA, MAY 02-06, 2005.

Der Kiureghian, A., Ditlevsen, O., 2009. Aleatory or epistemic? does it matter? Structural safety 31, 105–112.

Evans, J., Evans, J., Lall, P., Cornford, S., 1998. Thermomechanical failures in microelectronic interconnects. Microelectronics and Reliability 38, 523–529.

Fu, K., Chang, L., Ye, L., Yin, Y., 2016. Indentation stress-based models to predict fracture properties of brittle thin film on a ductile substrate. Surface and Coatings Technology 296, 46–57.

Fu, K., Yin, Y., Chang, L., Shou, D., Zheng, B., Ye, L., 2013. Analysis on multiple ring-like cracks in thin amorphous carbon film on soft substrate under nanoindentation. Journal of Physics D: Applied Physics 46, 505314.

Fukumasu, N.K., Souza, R.M., 2014. Numerical evaluation of cohesive and adhesive failure modes during the indentation of coated systems with compliant substrates. Surface and Coatings Technology 260, 266–271. The 41st International Conference on Metallurgical Coatings and Thin Films.

Gaillard, Y., Tromas, C., Woirgard, J., 2003. Pop-in phenomenon in MgO and LiF: observation of dislocation structures. Philosophical Magazine Letters 83, 553–561.

Gan, Z., Wang, C., Chen, Z., 2018. Material structure and mechanical properties of silicon nitride and silicon oxynitride thin films deposited by plasma enhanced chemical vapor deposition. Surfaces 1, 59–72.

Jian, S.R., Chen, G.J., Hsu, W.M., 2013. Mechanical Properties of Cu2O Thin Films by Nanoindentation. Materials 6, 4505–4513.

Jiang, Y., Wei, Y., Smith, J.R., Hutchinson, J.W., Evans, A.G., 2010. First principles based predictions of the toughness of a metal/oxide interface. International Journal of Materials Research 101, 8–15.

Kaloyeros, A.E., Jové, F.A., Goff, J., Arkles, B., 2017. Review—silicon nitride and silicon nitride-rich thin film technologies: Trends in deposition techniques and related applications. ECS Journal of Solid State Science and Technology 6, P691–P714.

Kot, M., Rakowski, W., Lackner, J.M., Łukasz Major, 2013. Analysis of spherical indentations of coating-substrate systems: Experiments and finite element modeling. Materials & Design 43, 99–111.

Leterrier, Y., Andersons, J., Pitton, Y., Månson, J.A.E., 1997. Adhesion of silicon oxide layers on poly(ethylene terephthalate). ii: Effect of coating thickness on adhesive and cohesive strengths. Journal of Polymer Science Part B: Polymer Physics 35, 1463–1472.

Li, H., Vlassak, J.J., 2009. Determining the elastic modulus and hardness of an ultra-thin film on a substrate using nanoindentation. Journal Of Materials Research 24, 1114–1126.

Li, X., Bhushan, B., Takashima, K., Baek, C., Kim, Y., 2003. Mechanical characterization of micro/nanoscale structures for MEMS/NEMS applications using nanoindentation techniques. Ultramicroscopy 97, 481–494. 4th International Conference on Scanning Probe Microscopy, Sensors and Nanostructures, LAS VEGAS, NEVADA, MAY 26-29, 2002.

Li, X., Diao, D., Bhushan, B., 1997. Fracture mechanisms of thin amorphous carbon films in nanoindentation. Acta Materialia 45, 4453–4461.

Lin, M.B., 2011. Introduction to VLSI systems: a logic, circuit, and system perspective. CRC press.

Lin, Y.C., Weng, Y.J., Pen, D.J., Li, H.C., 2009. Deformation model of brittle and ductile materials under nano-indentation. Materials & Design 30, 1643–1649.

Liu, J.n., Xu, B.s., Wang, H.d., Cui, X.f., Zhu, L.n., Jin, G., 2015. Measurement for mechanical behavior and fatigue property of Cu films by nanoscale dynamic load method. Materials & Design 65, 1136–1142.

Lofaj, F., Németh, D., 2017. Multiple cohesive cracking during nanoindentation in a hard wc coating/steel substrate system by fem. Journal of the European Ceramic Society 37, 4379–4388.

Mercier, D., Mandrillon, V., Parry, G., Verdier, M., Estevez, R., Bréchet, Y., Maindron, T., 2017. Investigation of the fracture of very thin amorphous alumina film during spherical nanoindentation. Thin Solid Films 638, 34–47.

Morin, P., Raymond, G., Benoit, D., Guiheux, D., Pantel, R., Volpi, F., Braccini, M., 2011. Study of stress in tensile nitrogen-plasma-treated multilayer silicon nitride films. Journal of Vacuum Science & Technology A 29.

Needleman, A., 1987. A continuum model for void nucleation by inclusion debonding. Journal of Applied Mechanics 54, 525–531.

Nieva, N., Arreguez, C., Carrizo, R., Molé, C.S., Lagarrigue, G., 2012. Bonding strength evaluation on metal/ceramic interfaces in dental materials. Procedia Materials Science 1, 475–482.

Pelegri, A.A., Huang, X., 2008. Nanoindentation on soft film/hard substrate and hard film/soft substrate material systems with finite element analysis. Composites Science and Technology 68, 147–155.

Raghavan, S., Schmadlak, I., Leal, G., Sitaraman, S.K., 2016. Mixed-mode cohesive zone parameters for sub-micron scale stacked layers to predict microelectronic device reliability. Engineering Fracture Mechanics 153, 259–277.

Saha, R., Nix, W.D., 2002. Effects of the substrate on the determination of thin film mechanical properties by nanoindentation. Acta Materialia 50, 23–38.

Sakai, M., 2009. Substrate-affected indentation contact parameters of elastoplastic coating/substrate composites. Journal of Materials Research 24, 831–843. doi:`10.1557/jmr.2009.0102`.

Scafidi, P., Ignat, M., 1998. Cracking and loss of adhesion of Si3N4 and SiO2 : P films deposited on Al substrates. Journal Of Adhesion Science And Technology 12, 1219–1242.

Shieu, F., Shiao, M., 1997. Measurement of the interfacial mechanical properties of a thin ceramic coating on ductile substrates. Thin Solid Films 306, 124–129.

Sinha, A., Levinstein, H., Smith, T., 1978. Thermal-Stresses and Cracking Resistance Of Dielectric Films (SIN, Si3N4, and SiO2) On Si Substrates. Journal of Applied Physics 49, 2423–2426.

Soh, M.T.K., Fischer-Cripps, A.C., Savvides, N., Musca, C.A., Faraone, L., 2006. Nanoindentation of plasma-deposited nitrogen-rich silicon nitride thin films. Journal of Applied Physics 100, 024310.

Tekin, T., 2011. Review of packaging of optoelectronic, photonic, and mems components. IEEE Journal of selected topics in quantum electronics 17, 704–719.

Tvergaard, V., Hutchinson, J.W., 1992. The relation between crack growth resistance and fracture process parameters in elastic-plastic solids. Journal of the Mechanics and Physics of Solids 40, 1377–1397.

Wang, Q., Zhou, F., Yan, J., 2016. Evaluating mechanical properties and crack resistance of CrN, CrTiN, CrAlN and CrTiAlN coatings by nanoindentation and scratch tests. Surface & Coatings Technology 285, 203–213.

Xiang, D., Xia, H., Yang, W., Mou, P., 2019. Parametric study and residual gas analysis of large-area silicon-nitride thin-film deposition by plasma-enhanced chemical vapor deposition. Vacuum 165, 172–178.

Xu, X.P., Needleman, A., 1993. Void nucleation by inclusion debonding in a crystal matrix. Modelling and Simulation in Materials Science and engineering 1, 111.

Yamakov, V., Saether, E., Philips, D., Glaessen, E., 2006. Molecular-dynamics simulation-based cohesive zone representation of intergranular fracture processes in aluminum. Journal of the Mechanics and Physics of Solids 54, 1899–1928.

Zhang, S., Sun, D., Fu, Y., Du, H., 2005. Toughness measurement of thin films: a critical review. Surface and Coatings Technology 198, 74–84.